HAL
open science

In situ elaboration of a binary Ti–26Nb alloy by selective laser melting of elemental titanium and niobium mixed powders

Marie Fischer, David Joguet, Guillaume Robin, Laurent Peltier, Pascal Laheurte

To cite this version:

Marie Fischer, David Joguet, Guillaume Robin, Laurent Peltier, Pascal Laheurte. In situ elaboration of a binary Ti–26Nb alloy by selective laser melting of elemental titanium and niobium mixed powders. Materials Science and Engineering: C, 2016, 62, pp.852-859. 10.1016/j.msec.2016.02.033 . hal-01993725

HAL Id: hal-01993725

https://hal.science/hal-01993725v1

Submitted on 25 Jan 2019

HAL is a multi-disciplinary open access archive for the deposit and dissemination of scientific research documents, whether they are published or not. The documents may come from teaching and research institutions in France or abroad, or from public or private research centers.

L'archive ouverte pluridisciplinaire **HAL**, est destinée au dépôt et à la diffusion de documents scientifiques de niveau recherche, publiés ou non, émanant des établissements d'enseignement et de recherche français ou étrangers, des laboratoires publics ou privés.

In situ elaboration of a binary Ti–26Nb alloy by selective laser melting of elemental titanium and niobium mixed powders

M. Fischer [a], D. Joguet [b], G. Robin [a], L. Peltier [c], P. Laheurte [a,*]

[a] Laboratoire d'Etude des Microstructures et de Mécanique des Matériaux LEM3 (UMR CNRS 7239), Université de Lorraine, Ile de Saulcy, F-57045 Metz, France
[b] Laboratoire d'Etudes et de Recherches sur les Matériaux, les Procédés et les Surfaces LERMPS, Université de Technologie de Belfort Montbéliard, Sevenans, 90010 Belfort, France
[c] Laboratoire d'Etude des Microstructures et de Mécanique des Matériaux LEM3 (UMR CNRS 7239), Ecole Nationale Supérieure d'Arts et Métiers, F-57078 Metz, France

A B S T R A C T

Ti–Nb alloys are excellent candidates for biomedical applications such as implantology and joint replacement because of their very low elastic modulus, their excellent biocompatibility and their high strength. A low elastic modulus, close to that of the cortical bone minimizes the stress shielding effect that appears subsequent to the insertion of an implant. The objective of this study is to investigate the microstructural and mechanical properties of a Ti–Nb alloy elaborated by selective laser melting on powder bed of a mixture of Ti and Nb elemental powders (26 at.%). The influence of operating parameters on porosity of manufactured samples and on efficacy of dissolving Nb particles in Ti was studied. The results obtained by optical microscopy, SEM analysis and X-ray microtomography show that the laser energy has a significant effect on the compactness and homogeneity of the manufactured parts. Homogeneous and compact samples were obtained for high energy levels. Microstructure of these samples has been further characterized. Their mechanical properties were assessed by ultrasonic measures and the Young's modulus found is close to that of classically elaborated Ti–26Nb ingot.

1. Introduction

Metastable beta titanium alloys Ti–xNb (22% < x < 27% atomic %) are excellent candidates for biomedical applications such as implantology and osteoarticular surgery because of their very low elastic modulus, their excellent biocompatibility and their high strength [1–5]. A modulus of elasticity similar to that of the cortical bone is particularly appreciated in the manufacture of implants and prostheses because it allows to minimize the discontinuity in elastic properties at the implant–bone interface [6,7] and thus to reduce the stress shielding phenomenon following a joint replacement or the placing of an implant.

Moreover, typical surgical implant alloys and pure metals have been widely studied and classified. The characterization of the chemical biocompatibility of a material is related to its corrosion resistance and to the toxicity of the released ions in the body. Steinemann [8,9] established a classification of metallic elements and alloys commonly used for implants as function of their toxicity and expected tissue reaction. Vanadium, nickel and cobalt are in the toxicity group, iron, aluminum and Co–Cr and 316L alloys are in the sequestration group and titanium, niobium, tantalum, platinum and zirconium are in the inertness/vital group. Gepreel et al. and Rao et al. [10,11] deduced that the ideal biomaterial should possess good biological biocompatibility by being free of toxic elements. Therefore, they report that stainless steel, Co–Cr-based and Ti–6Al–4V alloys are not ideal to be used for long term implantation in the human body from the biological point of view due to their high content in cytotoxic elements. On the other hand, alloys containing Ti or Nb could be beneficial for implantation. Other authors [12–16] studied cytotoxicity by testing cell growth and viability on titanium alloys containing β-stabilizing elements: Cremasco et al. detected no toxic effect of the Ti–Nb–X system (X = Sn, Ta, Zr) and Park et al. studied numerous binary Ti–A alloys (A being Cu, Al, V, Mn, Zr, Nb, Mo…) and showed that Ti–xMo and Ti–xNb are the least cytotoxic of all and showed the highest cell viability.

The elaboration of implantable medical devices (IMD) in Ti–Nb from additive manufacturing is intended to provide custom made implants that can be qualified as biomimetic insofar as shape and elastic properties of the implant and bone will be close. Selective laser melting (SLM) is an additive manufacturing process that allows the production of three dimension (3D) parts with complex shapes directly from metallic powders. It presents several significant advantages compared to the conventional fabrication methods. The use of selective laser melting however requires verifying that the steps of manufacturing of the powder and the laser fusion permit to retain the properties of the initial alloy. Powder and its characteristics are therefore essential. Some authors have studied β-titanium alloys after SLM processing and have obtained encouraging results [17–20]. Nonetheless most materials, in a powder form are still scarce or even commercially unavailable. It is the case for Ti–Nb alloys. Indeed, the powders are generally obtained from a pre-alloyed material that is converted into powder by gas atomization or plasma arc to obtain spherical particles with a particle size between

20 and 100 μm. The high fusion temperature of Ti–Nb alloys makes it very complex to produce powders with this method.

In this work we sought to develop and study a new method to manufacture parts made in an alloy elaborated, in situ, from a mixture of elemental powder. Attempts to develop alloys in situ, with this type of method, are still few. An example is the study of Zhang et al. on NiTi [21] prepared from spherical powder obtained by gas atomization of Ti and Ni. The authors studied the effect of the scanning speed on microstructure and compactness. Another example is the study by Vrancken et al. [22] with the in situ elaboration of beta titanium from Ti–6Al–4V and Mo powders. Using parameters optimized for Ti–6Al–4V, Mo particles melted only partially but they were still able to retain the β phase after rapid cooling.

Here, Ti–26 at.% Nb alloy is manufactured from Ti powder and Nb powder by directly melting a mixture of non-spherical elemental powders under the laser beam. The influence of process parameters on homogeneity, compactness and elastic properties of the alloy is investigated.

2. Materials and methods

2.1. Material

Elemental T40 pure titanium and pure niobium powders, bought from supplier BAOJI DOUBLE WEI TITANIUM INDUSTRY CO. LTD, obtained from ball-milling processes, were used in this work. They present irregular morphologies (Fig. 1a) and different size distributions (Fig. 1b).

The size distributions of the powders used as precursor material were measured by laser diffraction for particle size analysis with MASTERSIZER 2000, Malvern Instruments Ltd., UK equipped with a wet dispersion unit (Hydro 2000). This technique is based on the deviation of light by the particles: as they flow in front of the laser beam, light is deviated by an angle inversely proportional to their size and with an intensity proportional to their size. Analysis of the measurements leads to the size distribution of powder in terms of volume and quantity (ISO 13320:2009).

The size distribution of titanium particles was $D_{10} = 26$ μm, $D_{50} = 62$ μm and $D_{90} = 118$ μm and as received niobium particles sizes ranged from $D_{10} = 12$ μm to $D_{90} = 100$ μm with $D_{50} = 44$ μm. Considering the respective fusion temperature of titanium and niobium of 1668 °C and 2477 °C, better melting and better Nb diffusion in Ti was expected with Nb particles smaller than Ti particles. This strategy has also been used in the study from Vrancken et al. [22] for alloying Ti–6Al–4V powder ($d_{50} = 34$ μm) with Mo particles (d = 5–10 μm). Hence, Nb powder was sifted to reach a narrower distribution with $D_{10} = 9$ μm, $D_{50} = 25$ μm and $D_{90} = 50$ μm. Fig. 1b presents the titanium and niobium particles size distributions used in this study.

The powders were mixed with weight proportions Ti:Nb = 59.5:40.5, namely 74:26 atom proportions. The chemical composition of the mixture is given in Table 1. The titanium and niobium contents were measured by inductively coupled plasma atomic emission spectroscopy. The carbon and the oxygen were analyzed by fusion method and infrared detection, and the nitrogen and the hydrogen by fusion and conduction.

3. Methods

All the SLM specimens were prepared using a Realizer SLM 250 machine equipped with an IPG Ytterbium fiber laser (YLR-400) at a wavelength of 1070 nm and maximum power of 400 W. The processing environment consists of a controlled argon atmosphere aimed to keep oxygen content inferior to 0.5%. Parts are produced layer by layer until a three-dimensional object is formed. The powder layer thickness is controlled by the displacement in the z-direction of the build platform Fig. 2.

In the used equipment, the laser spot (Ø 40 μm) travels in a discontinuous scan mode on the surface thus, the scanning speed v (Eq. (1)) [23,24] is described by p_{dist}, the distance between points (mm); t_{expo}, the exposure time (s); and v_x, the travel speed between two points estimated at 2500 mm/s. The laser remains on during the flight in between points.

$$v = \frac{P_{dist}}{\frac{P_{dist}}{v_x} + t_{expo}} \tag{1}$$

A cross hatching laser scanning strategy where the direction of scanning is switched from x to y (and y to x) for successive layers was adopted. However, the laser scanning strategy is defined differently in the volume border corresponding to the outer boundary and in the volume area corresponding to the core of the part (Fig. 2). Indeed, a single scan track defines the edges whereas, in the core of the part, scanning strategy can be described with the hatch distance *s* (mm): the distance between scan tracks (Fig. 3).

Scanning parameters can be used to control the energy delivered (Eq. (2)) to the powder bed ($\overline{E}_f$) ([24]). The dimensions of the built parts are taken into account with L (mm) and l (mm) its length and width. Here, the powder mixture was melted layer by layer to form cubic specimens with dimensions 8 mm × 8 mm × 8 mm and parallelepiped specimens with dimensions 8 mm × 8 mm × 16 mm. The energy

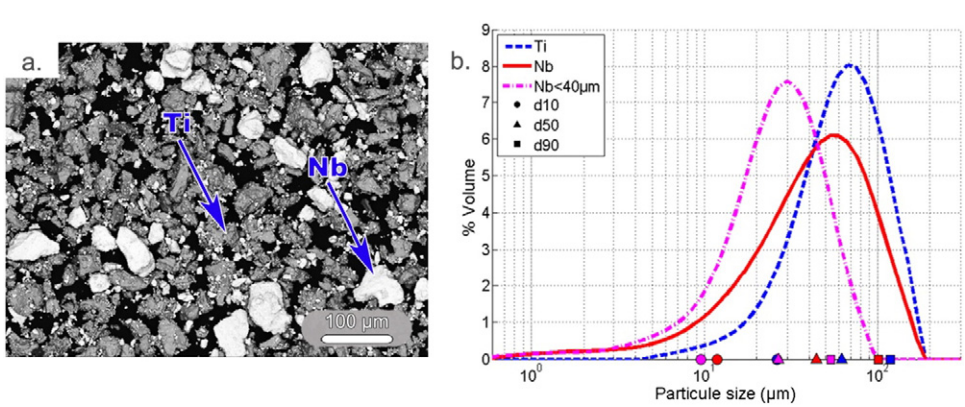

Fig. 1. Characteristics of the mixture of elemental Ti and Nb powders: (a) SEM image, (b) particle size distribution.

Table 1
Chemical composition (wt.%) of the powder mix.

Element	Ti	Nb	C	S	H	N	O
Incertitude (wt.%)	(±1.7)	(±1.2)	(±0.003)	(±0.001)	(±0.0012)	(±0.002)	(±0.02)
Mixed powder (wt.%)	58.2	38.6	0.029	0.007	0.0056	0.007	0.46

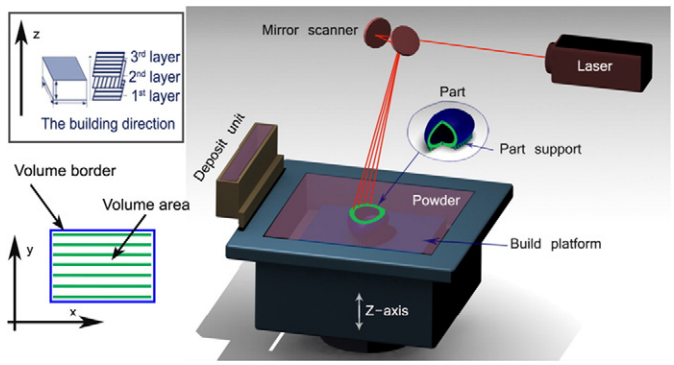

Fig. 2. Principle of selective laser melting process.

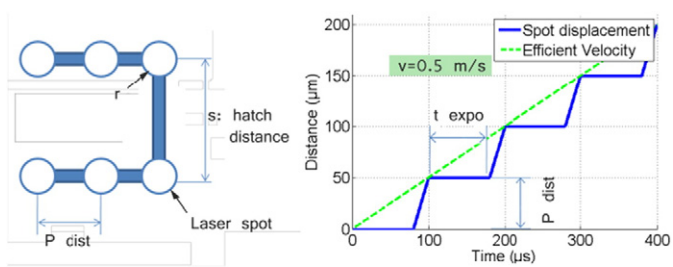

Fig. 3. Spot displacement kinetic with $t_{expo} = 80$ µs and $P_{dist} = 50$ µm.

density as described in Eq. (2) is defined for the area where all process parameters are included [24].

$$\overline{E}_f = \frac{P\left(t_{expo} + \frac{p_{dist}}{v_x}\right)}{S.p_{dist} \times t} \left({}^{J}/_{mm^3}\right) \tag{2}$$

In this study, scanning parameters were chosen in order to cover a large range of energies, from 39 J/mm^3 to 1467 J/mm^3: laser power: 120 W–360 W, hatch distance: 0.01 mm–0.1 mm, distance between points: 0.02 mm–0.065 mm, exposure time 20 µs–100 µs (Table 2). Layer thickness (t) was set at 30 µm in all the experiments and the top powder layer, being melted, corresponds to the position of the beam waist.

Table 2
Parameter level used in this study.

No.	Power (W)	Hatch distance (mm)	Distance between points (mm)	Exposure time (µs)	Energy density (J/mm^3)
1	120	0.100	0.035	20	39
2	120	0.060	0.020	20	93
3	120	0.080	0.035	90	148
4	220	0.040	0.065	50	214
5	360	0.040	0.065	80	489
6	220	0.020	0.040	100	1063
7	220	0.010	0.050	80	1467

Porosity and unmelted niobium content were the main criterions for validation of the process parameters. Niobium particles content was evaluated by X-ray microtomography and porosity was evaluated by image analysis of optical micrographs and microtomography. X-ray microtomography (Easytomnano RXsolutions) coupled to software Avizo allowed 3D mapping of the porosities, the determination of pores morphology and non-alloyed elements locations of our different samples. With this non-destructive method we can analyze singularities of a size less than the micro-CT accuracy.

X-ray diffraction analyses were conducted with a Cu Kα source (λ = 0.1540 nm) on selected samples to verify the elaboration of a β Ti–26Nb alloy. Results were compared with diffractograms simulated with the CaRine Crystallography software from the lattice parameter found in the literature [25]. Moreover, EDX analyses were performed and microstructure was observed in optical microscopy after grinding and etching with Kroll's reagent. The carbon and the oxygen were analyzed by the fusion method and infrared detection, the nitrogen and the hydrogen by fusion and conduction methods.

To assess the mechanical properties, in particular Young's modulus, of the selected samples, an ultrasonic method was used. This method consisted in measuring the time of flight of the wave propagating through the material to deduce its Young's modulus.

The sample, prepared with parallel faces, is directly placed in contact between two transducers: an emitter and a receiver (Fig. 4). Two couples of transducers are used to propagate through the sample longitudinal and transversal waves respectively. The central frequency of these transducers is equal to 5 MHz. The nominal element size of these

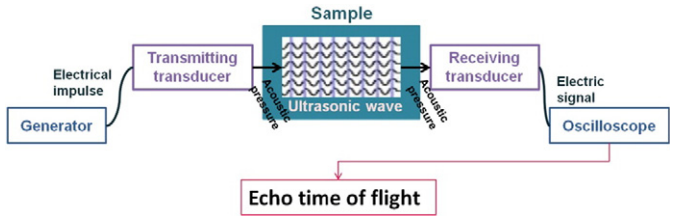

Fig. 4. Experimental setup for ultrasonic measurements.

transducers is 0.25 in. An electrical pulse generator connected to the transducer allows the generation of an acoustic pressure that propagates as a pulse wave through the sample with a 100 Hz pulse repetition frequency. Then, the other transducer receives the wave on its surface and converts it into an electrical signal that can be shown on an oscilloscope. Time sampling of the acquisition is 0.5 ns. The longitudinal (V_L) and transversal (V_T) wave velocities are then directly determined. This allowed deducing the mechanical properties [26]: Young modulus (E), shear modulus (G), and Poisson's ratio (υ) of the samples.

$$E = \frac{\rho V_T^2\left(3V_L^2 - 4V_T^2\right.}{V_L^2 - V_T^2} \tag{3}$$

$$G = \rho V_T^2 \tag{4}$$

$$\upsilon = \frac{\frac{1}{2}\left(V_L^2 - 2V_T^2\right)}{V_L^2 - V_T^2} \tag{5}$$

4. Results and discussion

4.1. Porosity and homogeneity

Porosity analyses provide information about the behavior of the material in the melting pool during laser scan. Fig. 5 presents a general view of two extreme samples obtained during this study.

It is clear that the porosities observed on the samples present different morphologies and sizes but the repartition remains homogeneous. Fig. 5a shows the presence of many partially melted niobium particles and a lot of porosities with important size. Fig. 5b presents a relatively homogeneous structure and few remaining Nb particles.

Porosity percentage was evaluated in the volumes and Fig. 7 presents the porosity content as a function of the energy delivered to the surface. To evaluate the homogeneity of the elaborated TiNb alloys, the ratio in mass of unmelted niobium to introduced niobium has been calculated from results of tomographic analyses (Fig. 6).

Both tomography and image analysis measurement methods show similar results. A tendency in porosity content was clearly shown with equation $p = 73.35 \times {E_f}^{-0.542}$ and confirms the importance of energy in the SLM outcome. From energy of 210 J/mm^3, porosity content stabi-

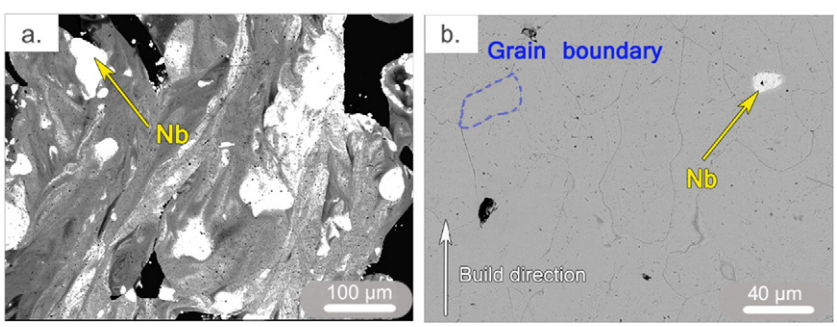

Fig. 5. SEM micrographs of sample (a) no. 1 and (b) no. 4.

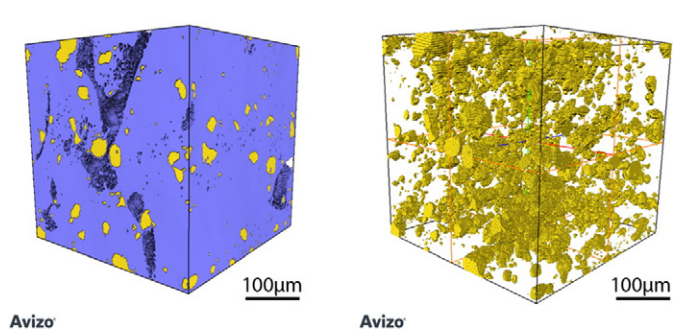

Fig. 6. Tomographic reconstruction of a volume in sample 1 with 19.7% porosity and 20.3% Nb particles; (a) full volume with TiNb alloy (blue), Nb particles (yellow), voids (hollow)and (b) Nb particles in the volume.

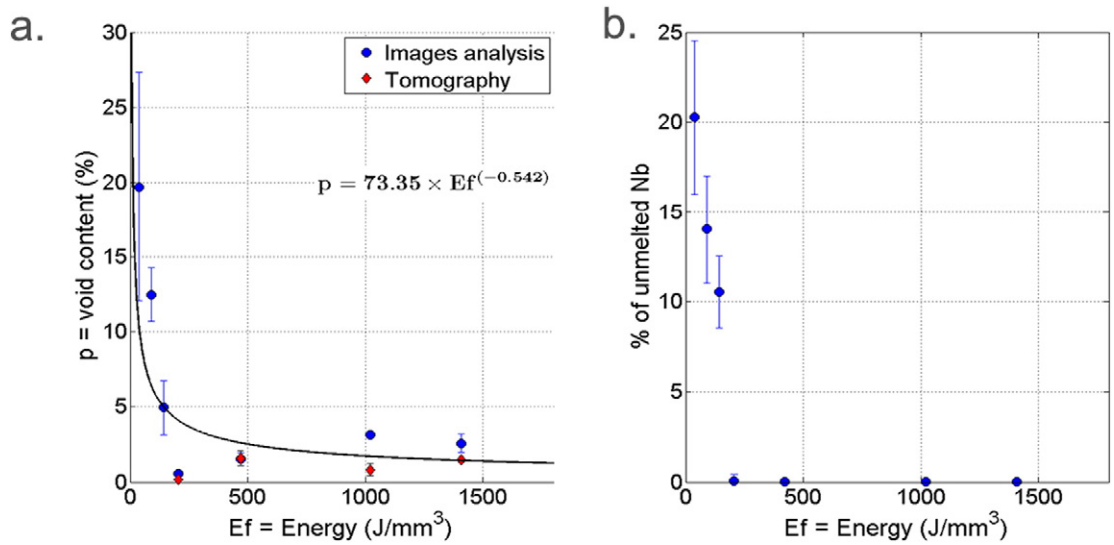

Fig. 7. Representation of (a) porosity content (b) % of unmelted niobium versus energy density, measures were replicated 5 times (error bars correspond to the standard deviation).

lizes and reaches a value inferior to 3%. It can be noticed however that there is a slight increase of the porosity at energies higher than this optimum which may be caused by an excess of energy. Indeed to high energy may have consequences on the quality of the upper surface of the melt pool due to convective motions in the liquid pool [20,27]. The resulting irregular surface will thus inhibit the proper spread of the next powder layer and favor porosity. Another hypothesis is that for sample 4, the delivered energy is adapted to a complete melt where porosity is minimized however when the level of energy goes too high the porosity increases due to the increase of the vaporization phenomenon resulting in pores trapped in the matrix or in irregularities of the surface also inhibiting the proper spread of the next powder layer [28–30].

Partially molten niobium content after laser scan shows a decreasing tendency similar to porosity content. Unmolten Nb particles represent less than 1% of the total amount of the Nb mass in the alloy when the energy used is more than 200 J/mm^3. The observed characteristics are very close for all the last four specimens.

Volume area of sample 4 (Fig. 8) presents few unmelted niobium nodules with relatively insignificant size. EDX quantification was carried out to evaluate the diffusion phenomenon and is presented on Fig. 8. EDX quantification shows a relatively homogenous alloys with Ti–(40% mass)Nb as intended. The diffusion zone of niobium around the particle is narrowed to approximately 5 μm. It confirms the ability of the process to maintain the proportions of rough powders in a homogeneous manufactured alloy.

4.2. Phase and microstructure analysis

XRD pattern (Fig. 9) of powder, sample no. 1 (39 J/mm^3) and sample no. 4 (210 J/mm^3) permits to identify the phases present in the materials elaborated at different energy levels.

Two phases corresponding to hcp α titanium and bcc niobium were identified in the feedstock powder.

In the fabricated samples, when the applied energy increases, diffraction patterns show clearly the elimination of the α titanium phase. XRD has also been used by Zhuravleva et al. [31] to demonstrate the formation of a β-titanium in ball-milling of Ti and Nb mixed powders.

In the sample manufactured at 39 J/mm^3, which is porous and non-homogeneous, both bcc niobium and bcc β Ti–26Nb phases are present. The Nb peaks result from the niobium nodules present in the alloy matrix. Furthermore, the peaks for higher 2θ may correspond to bcc Nb or Ti–26Nb as lattice parameters of Nb are close to that of metastable β TiNb which makes them difficult to differentiate. Or since they are slightly wider than usual peaks, they may correspond to both the Nb nodules and the TiNb alloy.

The only present phase in the sample fabricated at 210 J/mm^3 is β Ti–26Nb phase. This information confirms that the fabricated TiNb alloy contains more than 25 at.% Nb [25] otherwise, α″ phase would be found. Plus, this shows that the cooling speeds are high enough to retain a beta-metastable phase at room temperature. Lattice parameter was recalculated with the experimental diagram and is $a = 3.289 \pm 0.001$ Å and is consistent with the β-metastable Ti–26Nb alloy parameter. However, this information alone would not be sufficient to prove the exact composition of the alloy because the beta lattice parameter a does not vary greatly with Nb content [25]. Here, the exact composition is mainly confirmed by the EDX quantification shown in Fig. 8.

Examination of the fabricated alloys was then continued on sample no. 4 only, manufactured at energy of 210 J/mm^3. This level of energy allows the elaboration of an homogeneous, nonporous alloy and use of higher energy is not necessary as it would lead to a more time and energy consuming process.

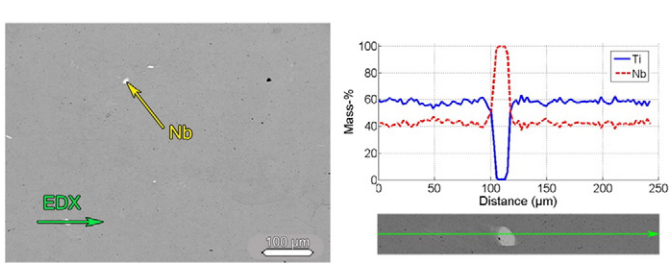

Fig. 8. SEM micrograph of sample no. 4 directly elaborated in situ without thermal treatment and EDX quantification near a niobium nodule of in situ elaborated sample no. 4.

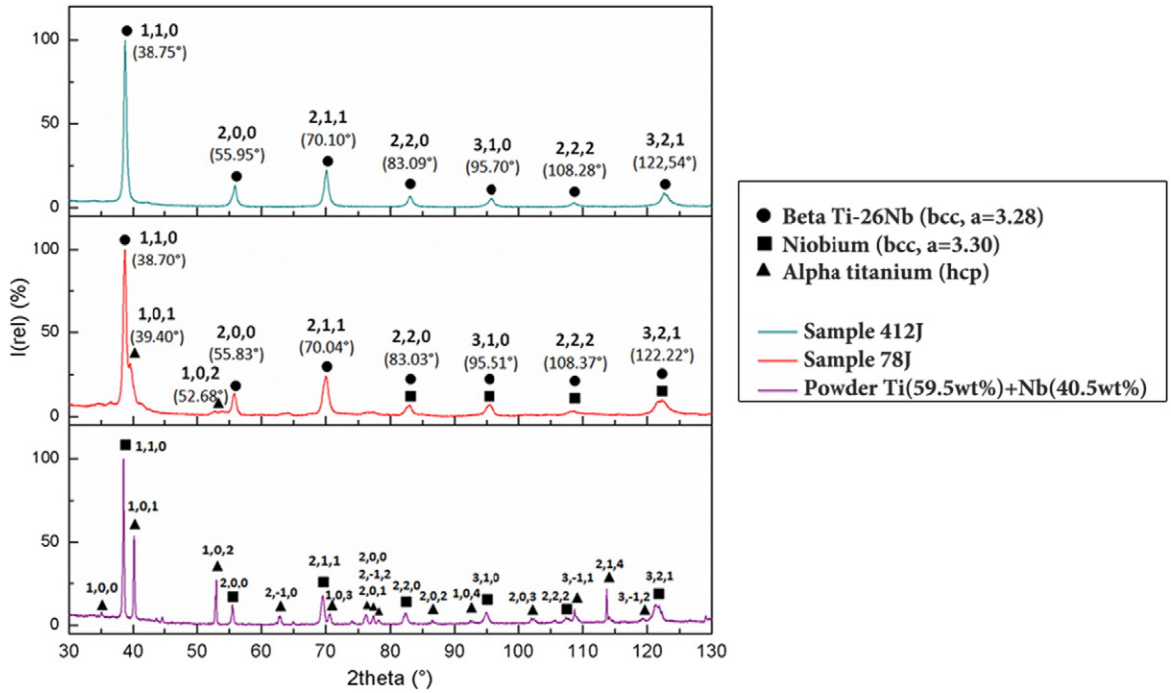

Fig. 9. XRD pattern of different energy level.

The microstructure is composed of large beta grains, mainly oriented along the building direction (Fig. 10). This microstructure is very different than that observed in selective laser melted Ti–6Al–4V or other titanium alloys [32,33]. Non-columnar elongated grains are formed with lengths up to 100 μm. This observation points out that the grain size in the z-direction is greater than the layer thickness. This is the result of an optimal remelting of the previous layer and of a diffusion phenomenon and shows the influence of previously elaborated layers on microstructural properties.

In the SEM images, the melt pool boundaries are visible. Most grains grew epitaxially, perpendicular and across the melt pool boundaries towards the top center of each melting track. This growing pattern is comparable to that obtained by Vrancken et al. [22] for their in situ elaboration of β titanium alloy from mixture of Ti6Al4V-ELI powder with 10 wt.% Mo powder.

Moreover, along the melt pool boundaries, micro-segregation is visible and presents in the form of short lines less than 1 μm wide perpendicular to the scan tracks limits. This chemical heterogeneity is probably caused by the remelting–resolidification of the previously deposited layer. The grain structure is however not influenced by this micro-segregation.

Texture was analyzed on each cross section with EBSD in order to highlight a preferred crystallographic orientation. The crystal growth occurs along the maximum temperature gradient in the direction

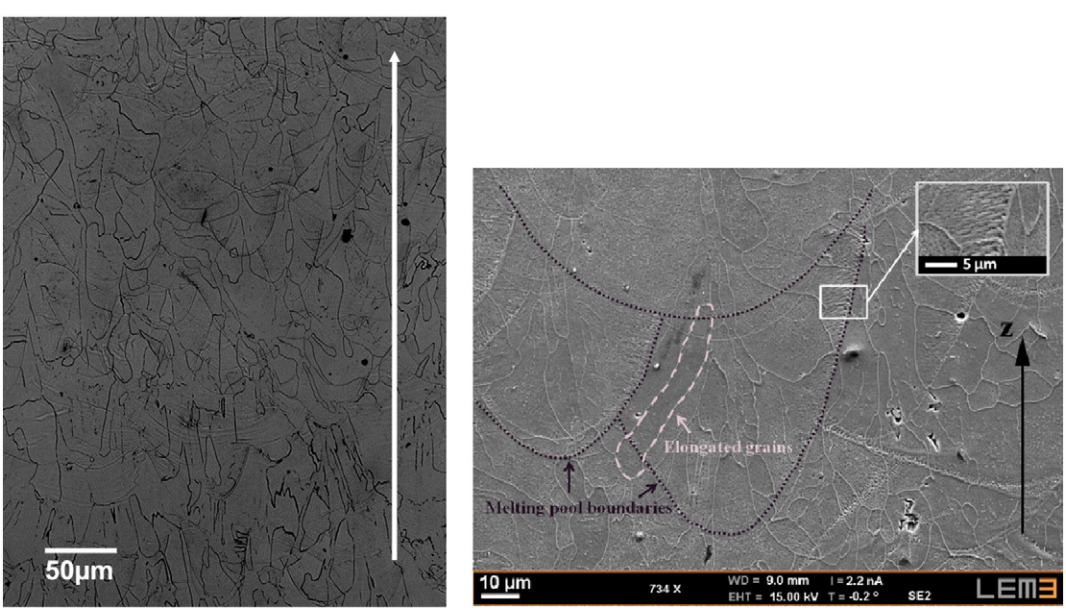

Fig. 10. Microstructures observed in the lateral plane (xz cross-section), with optical microscopy (left) and with scanning electron microscopy (right), z being the building direction.

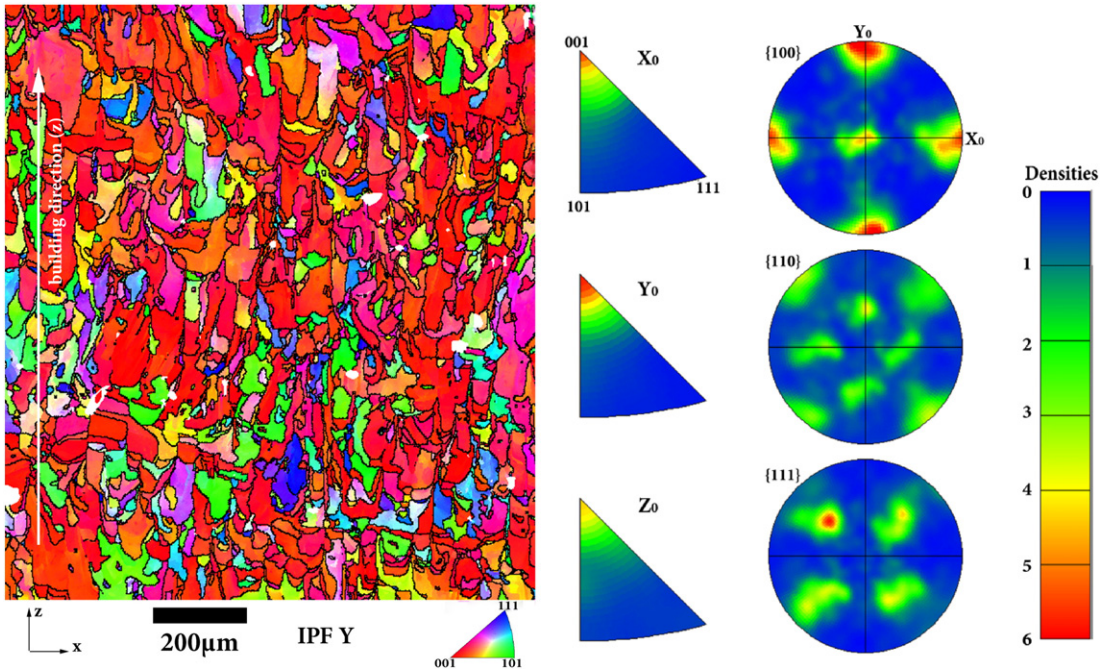

Fig. 11. IPFY EBSD map (xy cross-section) represented with respect to the y direction showing multiple grain orientations, inverse pole figure and pole figure for xz cross section of sample no. 4.

<100>, which is the easy-growth direction for the body centered cubic crystals. For laser additive manufacturing processes, this growth direction generally matches with the building direction [34].

Here, the EBSD analyses (Fig. 11) revealed a pole figure identical to the standard stereographic projection of the cubic crystal. It corresponds to an orientation {001}<100>. In this case, the plane (001) of the planes family {100} is parallel to the construction surface thus perpendicular to the building direction and the pole figure presents a direction [001] parallel to the building direction. Moreover, there is also a direction of the family <100> parallel to x and one parallel to y.

In the sample, most of the grains are stacked this way {001}<100>. The system of axes of the sample is identical to that of the single bcc crystal.

4.3. Mechanical characterization

Microhardness tests were carried out along the x and z axes. Hardness is constant and comparable for both axes with $HV_{0.3(x)} = 268 \pm 5$ and $HV_{0.3(y)} = 266 \pm 5$. This proves the homogeneity of the alloy in terms of mechanical properties.

The mechanical properties of the samples, in particular Young's modulus, are determined thanks to an ultrasonic method. Majumdar et al. [26] discussed the accuracy of ultrasonic measures and affirmed that because the velocity of ultrasonic waves in the material is directly related to the elastic properties and the density of the solid, the elastic modulus of the material measured by ultrasound is a correct representation of the bulk material properties. The SLM elaborated Ti–26Nb alloy was measured along with CP Ti bar and Ti–26Nb ingot for reference and comparison. Plus, in the SLM sample, the measures were made in the three directions to verify the absence of anisotropy (Table 3).

Table 3
Mechanical properties measured by ultrasound.

Material		ρ (kg/m^3)	V_L (m/s)	V_T (m/s)	E (GPa)	G (GPa)	υ
CP Ti (bar)		4540	5648 ± 9	3173 ± 3	116.1 ± 0.4	45.7 ± 0.1	0.27
Ti–26Nb (ingot)		5609	4745 ± 6	2130 ± 3	69.9 ± 0.2	25.4 ± 0.1	0.37
Ti–26Nb SLM in situ	x	5609	4361 ± 12	2271 ± 7	76.0 ± 0.4	28.9 ± 0.2	0.36
	y	5609	4304 ± 12	2302 ± 7	77.2 ± 0.4	29.7 ± 0.2	0.39
	z	5609	4763 ± 6	2262 ± 3	77.7 ± 0.2	28.6 ± 0.1	0.35

The values of elastic modulus are analogous in the three directions of the manufactured sample with a mean value of 77 ± 1.4 GPa. This elastic modulus is significantly lower than that of pure titanium close to 120 GPa and is close to that of a Ti–26Nb solution treated ingot. By using this material with its lower modulus of elasticity for implants and prostheses, the stress shielding phenomenon appearing after implantation will be significantly reduced [35]. Moreover, the measures revealed no anisotropy of the mechanical properties. This can be explained by the texture of the polycrystal. Indeed, the sample resembling a stacking of crystals oriented {001}<100> whether the measure is made in the x, y or z direction, the measure direction remains perpendicular to the same family of planes {100}, thus all three directions are equivalent.

Tane et al. [36] studied the elastic properties of single crystals of beta-titanium TNTZ alloys in order to provides a new concept for the design of biomedical implants: Young's modulus in a specific direction of biomedical implants can be lowered by the orientation of a specific crystallographic direction in which the Young's modulus is low. They showed that for various beta-type titanium alloys, even thought the value of the modulus depends on the alloy composition, its evolution according to the direction presents the same behavior with the lowest modulus in the <100> direction and the highest in the <111> direction. Hence, biomedical implants with low Young's modulus can be achieved by the texture in which the crystallographic <100> direction is oriented along the loading direction in the human bone to prevent stress-shielding phenomena.

5. Conclusion

In this study, non-spherical niobium and titanium powders were mixed with weight proportions Ti:Nb = 59.5:40.5. They were melted with the selective laser melting process according to experiments with different parameters impacting the global energy delivered to the surface. We showed that:

1) Energy has a significant effect on porosity and homogeneity of the produced part. A homogeneous alloy can be obtained from energy levels of 200 J/mm^3 with very few Nb particles left and porosity content inferior to 3%.
2) The manufactured alloy is fully β with non-columnar but elongated grains perpendicular to the melting pool boundaries. Grains show an epitaxial growth with a texture {001}<100> favorable for a low modulus.
3) Overall, this study showed that it is possible to elaborate a homogeneous alloy from mixed powders and that the non-spherical shape is no obstacle for achieving homogeneity and compactness.
4) In situ alloying from elemental powders opens a wide range of composition adjustment possibilities. It could potentially be applied to any alloy whose powder is difficult to obtain. With this method, any alloy composition can be elaborated in few steps.

Acknowledgments

This study was funded through the FAPROM project by the Region Lorraine.

References

[1] P. Laheurte, F. Prima, A. Eberhardt, T. Gloriant, M. Wary, E. Patoor, Mechanical properties of low modulus beta titanium alloys designed from the electronic approach, J. Mech. Behav. Biomed. Mater. 3 (8) (Nov. 2010) 565–573.
[2] S. Miyazaki, H.Y. Kim, H. Hosoda, Development and characterization of Ni-free Ti-base shape memory and superelastic alloys, Mater. Sci. Eng. A 438–440 (Nov. 2006) 18–24.
[3] M. Niinomi, T. Akahori, M. Nakai, In situ X-ray analysis of mechanism of nonlinear super elastic behavior of Ti–Nb–Ta–Zr system beta-type titanium alloy for biomedical applications, Mater. Sci. Eng. C 28 (3) (Apr. 2008) 406–413.
[4] F. Sun, Y.L. Hao, S. Nowak, T. Gloriant, P. Laheurte, F. Prima, A thermo-mechanical treatment to improve the superelastic performances of biomedical Ti–26Nb and Ti–20Nb–6Zr (at.%) alloys, J. Mech. Behav. Biomed. Mater. 4 (8) (Nov. 2011) 1864–1872.
[5] A. Ramarolahy, P. Castany, F. Prima, P. Laheurte, I. Péron, T. Gloriant, Microstructure and mechanical behavior of superelastic Ti–24Nb–0.5O and Ti–24Nb–0.5N biomedical alloys, J. Mech. Behav. Biomed. Mater. 9 (May 2012) 83–90.
[6] S.H. Pettersen, T.S. Wik, B. Skallerud, Subject specific finite element analysis of stress shielding around a cementless femoral stem, Clin. Biomech. (Bristol, Avon) 24 (2) (Feb. 2009) 196–202.
[7] B. Piotrowski, A.A. Baptista, E. Patoor, P. Bravetti, A. Eberhardt, P. Laheurte, Interaction of bone-dental implant with new ultra low modulus alloy using a numerical approach, Mater. Sci. Eng., C 38 (May 2014) 151–160.
[8] S.G. Steinemann, Metal implants and surface reactions, Injury 27 (Jan. 1996) S/C16–S/C22.
[9] S.G. Steinemann, Corrosion of surgical implants — in vivo and in vitro tests, in: K.G.G. Winter, J. Lerary (Eds.), Evaluation of Biomaterials (Advances in Biomaterials), John Wiley & Sons, New York 1980, pp. 1–34.
[10] M. Abdel-Hady Gepreel, M. Niinomi, Biocompatibility of Ti-alloys for long-term implantation, J. Mech. Behav. Biomed. Mater. 20 (Apr. 2013) 407–415.
[11] S. Rao, Y. Okazaki, T. Tateishi, T. Ushida, Y. Ito, Cytocompatibility of new Ti Alloy Without Al and V by Evaluating the Relative Growth Ratios of Fibroblasts L929 and Osteoblasts MC3T3-El cells, vol. 41997 311–314.
[12] Y.-J. Park, Y.-H. Song, J.-H. An, H.-J. Song, K.J. Anusavice, Cytocompatibility of pure metals and experimental binary titanium alloys for implant materials, J. Dent. 41 (12) (Dec. 2013) 1251–1258.
[13] A. Cremasco, A.D. Messias, A.R. Esposito, E.A. de R. Duek, R. Caram, Effects of alloying elements on the cytotoxic response of titanium alloys, Mater. Sci. Eng. C 31 (5) (Jul. 2011) 833–839.
[14] K. Miura, N. Yamada, S. Hanada, T.-K. Jung, E. Itoi, The bone tissue compatibility of a new Ti–Nb–Sn alloy with a low Young's modulus, Acta Biomater. 7 (5) (May 2011) 2320–2326.
[15] M. Metikoš-Huković, A. Kwokal, J. Piljac, The influence of niobium and vanadium on passivity of titanium-based implants in physiological solution, Biomaterials 24 (21) (Sep. 2003) 3765–3775.
[16] R.E. McMahon, J. Ma, S.V. Verkhoturov, D. Munoz-Pinto, I. Karaman, F. Rubitschek, H.J. Maier, M.S. Hahn, A comparative study of the cytotoxicity and corrosion resistance of nickel-titanium and titanium-niobium shape memory alloys, Acta Biomater. 8 (7) (Jul. 2012) 2863–2870.
[17] S. Dadbakhsh, M. Speirs, G. Yablokova, J.P. Kruth, J. Schrooten, J. Luyten, J. Van Humbeeck, Microstructural analysis and mechanical evaluation of Ti–45Nb produced by selective laser melting towards biomedical applications.pdf, TMS2015 Annu. Meet. Suppl. Proc, 2015.
[18] G. Yablokova, S. Dadbakhsh, M. Speirs, A. Khangholi, Surface treatment of Ti–45Nb open porous structures towards biomedical applications : a modified approach, TMS2015 Annu. Meet. Suppl. Proc, 2015.
[19] K. Zhuravleva, M. Bönisch, K.G. Prashanth, U. Hempel, A. Helth, T. Gemming, M. Calin, S. Scudino, L. Schultz, J. Eckert, A. Gebert, Production of porous β-type Ti–40Nb alloy for biomedical applications: comparison of selective laser melting and hot pressing, Materials (Basel) 6 (12) (2013) 5700–5712.
[20] Y.J. Liu, X.P. Li, L.C. Zhang, T.B. Sercombe, Processing and properties of topologically optimised biomedical Ti–24Nb–4Zr–8Sn scaffolds manufactured by selective laser melting, Mater. Sci. Eng. A 642 (Aug. 2015) 268–278.
[21] B. Zhang, J. Chen, C. Coddet, Microstructure and transformation behavior of in-situ shape memory alloys by selective laser melting Ti–Ni mixed powder, J. Mater. Sci. Technol. 29 (9) (Sep. 2013) 863–867.
[22] B. Vrancken, L. Thijs, J.-P. Kruth, J. Van Humbeeck, Microstructure and mechanical properties of a novel β titanium metallic composite by selective laser melting, Acta Mater. 68 (Apr. 2014) 150–158.
[23] A. Masmoudi, R. Bolot, C. Coddet, Investigation of the laser–powder–atmosphere interaction zone during the selective laser melting process, J. Mater. Process. Technol. 225 (Nov. 2015) 122–132.
[24] D. Joguet, S. Costil, H. Liao, Y. Danlos, Porosity content control of CoCrMo and titanium parts by Taguchi method applied to selective laser melting process parameter, Rapid Prototyp. J. 1 (22) (Jan. 2016).
[25] H.Y. Kim, Y. Ikehara, J.I. Kim, H. Hosoda, S. Miyazaki, Martensitic transformation, shape memory effect and superelasticity of Ti–Nb binary alloys, Acta Mater. 54 (9) (May 2006) 2419–2429.
[26] P. Majumdar, S.B.B. Singh, M. Chakraborty, Elastic modulus of biomedical titanium alloys by nano-indentation and ultrasonic techniques—A comparative study, Mater. Sci. Eng. A 489 (1–2) (Aug. 2008) 419–425.
[27] J.-P. Kruth, G. Levy, F. Klocke, T.H.C. Childs, Consolidation phenomena in laser and powder-bed based layered manufacturing, CIRP Ann. Manuf. Technol. 56 (2) (Jan. 2007) 730–759.
[28] W. Di, Y. Yongqiang, S. Xubin, C. Yonghua, Study on energy input and its influences on single-track,multi-track, and multi-layer in SLM, Int. J. Adv. Manuf. Technol. 58 (9–12) (2012) 1189–1199.
[29] K.A. Mumtaz, P. Erasenthiran, N. Hopkinson, High density selective laser melting of Waspaloy®, J. Mater. Process. Technol. 195 (1–3) (Jan. 2008) 77–87.
[30] J.P. Kruth, L. Froyen, J. Van Vaerenbergh, P. Mercelis, M. Rombouts, B. Lauwers, Selective laser melting of iron-based powder, J. Mater. Process. Technol. 149 (1–3) (2004) 616–622.
[31] K. Zhuravleva, M. Bönisch, S. Scudino, M. Calin, L. Schultz, J. Eckert, A. Gebert, Phase transformations in ball-milled Ti–40Nb and Ti–45Nb powders upon quenching from the ß-phase region, Powder Technol. 253 (Feb. 2014) 166–171.
[32] L. Thijs, F. Verhaeghe, T. Craeghs, J. Van Humbeeck, J.-P. Kruth, A study of the microstructural evolution during selective laser melting of Ti–6Al–4V, Acta Mater. 58 (9) (May 2010) 3303–3312.
[33] E. Chlebus, B. Kuźnicka, T. Kurzynowski, B. Dybała, Microstructure and mechanical behaviour of Ti–6Al–7Nb alloy produced by selective laser melting, Mater. Charact. 62 (5) (May 2011) 488–495.
[34] M. Simonelli, Y.Y. Tse, C. Tuck, On the texture formation of selective laser melted Ti–6Al–4V, Metall. Mater. Trans. A 45 (6) (Feb. 2014) 2863–2872.
[35] M. Niinomi, Mechanical biocompatibilities of titanium alloys for biomedical applications, J. Mech. Behav. Biomed. Mater. 1 (1) (Jan. 2008) 30–42.
[36] M. Tane, S. Akita, T. Nakano, K. Hagihara, Y. Umakoshi, M. Niinomi, H. Nakajima, Peculiar elastic behavior of Ti–Nb–Ta–Zr single crystals, Acta Mater. 56 (12) (Jul. 2008) 2856–2863.